

Automatic segmentation of corneal endothelial cells from microscopy images

Anna Fabijańska

Lodz University of Technology, Institute of Applied Computer Science, 18/22 Stefanowskiego Str., 90-924 Lodz, Poland



ARTICLE INFO

Article history:

Received 30 March 2018

Received in revised form 1 July 2018

Accepted 14 August 2018

Available online 25 August 2018

Keywords:

Corneal endothelium

Cell segmentation

Iterative cell separation

Morphological processing

Neural network

ABSTRACT

The structure of the corneal endothelial cells can provide important information about the cornea health status. Particularly, parameters describing cell size and shape are important. However, these parameters are not widely used, because it requires segmentation of the cells from corneal endothelium images. Although several dedicated approaches exist, none of them is faultless. Therefore, this paper proposes a new approach to fully automatic segmentation of corneal endothelium images. The proposed approach combines a neural network which is thought to recognize pixels located at the cell boundaries, with postprocessing of the resulting boundary probability map. The postprocessing includes morphological reconstruction followed by coarse cell segmentation using local thresholding. The resulting cells are next separated from each other via iterative morphological opening. Finally, the region between cell bodies is skeletonized. The proposed method was tested on three publicly available corneal endothelium image datasets. The results were assessed against the ground truths and compared with the results provided by selected state-of-the-art methods. The resulting cell boundaries are well aligned with the ground truths. The mean absolute error of the determined cell number equals 6.78%, while the mean absolute error of cell size is at the level of 5.13%. Cell morphometric parameters were determined with the error of 5.69% for the coefficient of variation of cell side length and 11.64% for cell hexagonality.

© 2018 Elsevier Ltd. All rights reserved.

1. Introduction

The corneal endothelium is a monolayer on the posterior surface of the cornea. It regulates the dehydration of cornea by governing transport of fluid and solutes across the corneal structures that are required to assure the optical transparency. The layer is formed by closely packed, predominantly hexagonal cells of uniform size and the organization which resembles a honeycomb. In the young, healthy adults there are c.a. 3500 endothelial cells per square millimeter [1]. However, the cell density progressively decreases during the lifetime, ranging from about 6000 cells/mm² at the birth to about 2300 cells/mm² at the age of 85.

The organization of the cells in the corneal endothelium is of great interest for ophthalmologists because it can provide important diagnostic information about the cornea health status or indicate some corneal diseases. Particularly, different pathological conditions may speed up the loss of endothelial cells and thus abnormally decrease cell density. The loss of cells deteriorates the

hexagonal pattern. The damaged endothelial tissue does not regenerate. Therefore, neighboring cells expand and migrate to fill void space corresponding to the destroyed cells. This leads to unpredictable cell elongation, thinning and size increase. Cell density is thus one of the most important parameters describing the corneal endothelium health condition. Other morphometric parameters useful for assessment of corneal endothelium aging and health status are cell hexagonality and the coefficient of variation of cell size.

In the everyday clinical routine, the condition of corneal endothelium is usually assessed qualitatively, by visual inspection of corneal endothelium images obtained with a specular microscope. The quantitative assessment using the morphometric parameters and cell geometry analysis is not very common. It is because it requires segmentation of all cells present in the corneal endothelium image. Although several approaches to segmentation of corneal endothelium images have been proposed none of them is faultless. Therefore, to date, obtaining reliable cell contours still requires manual delineation (or at least extensive editing) of cell boundaries. Since there are thousandths of endothelial cells per square millimeter, their manual segmentation is a very

E-mail address: anna.fabijanska@p.lodz.pl

time-consuming activity. Therefore providing a reliable method for automatic segmentation of endothelial cells is still a vital problem.

The automatic segmentation of corneal endothelial cells is not a trivial task. The challenges are caused by a moderate quality of specular microscopy images which exhibits by inhomogeneous illumination. This, in turn, causes lower contrast and varying background intensities. As a result, some of the cell boundaries are difficult to recognize even by a medical expert. Because of these reasons, none of the existing approaches to endothelial cells automatic segmentation is faultless and thus manual editing of the results is required.

To the author's best knowledge, the first approach to automated corneal endothelial cell analysis was proposed about 25 years ago by Nadachi and Nunokawa [2] who suggested using image thresholding followed by scissoring and morphological thinning. Missing boundaries were next edited manually. Similar approaches were also used by Sanchez [3] who preceded thresholding by a scale-space filtering and Ayala et al. [4] in their work on assessment of corneal endothelium health status using granulometric moments. Mahzoun [5] proposed to perform cell segmentation by hexagon detection using directional filters followed by binarization, and thinning. A similar approach was also used in [6], where the authors applied different directional filters and provided a method for background intensity normalization.

Since the mosaic of corneal endothelial cells in confocal images manifests itself as bright regions separated by visibly darker lines many authors have tried to perform cell segmentation using the watershed algorithm. Attempts have been made to draw the watershed lines along cell boundaries in the inverted corneal endothelium image. Firstly, Vincent et al. [7] proposed an approach based on marker-driven cell segmentation. Their approach, however, may require the manual placing of seeds within each cell, since finding seeds automatically is up to date problematic. To avoid this shortcoming, in [8,9] it was proposed to additionally constrain watershed segmentation by a distance map. The slightly different approach was proposed by Bullet et al. [10] who built watersheds on distance map, but then separated fused cells using Voronoi diagrams. However, as shown in [11] these methods are very sensitive to parameter setting and thus require some experimentation before optimal results are obtained. Recently, Selig et al. [12] have proposed to use stochastic watershed in order to avoid user interaction and empirical setting and adjustment of parameters. Dagher and El Tom [13] used watershed region contours to initialize multiple balloon snakes. Similar, multiple active contour approach was also proposed in [14], where multiple snake active contours are evolving starting from circular regions obtained by thresholding. The latter two approaches are fully automatic and do not require user interaction.

A lot of effort into the problem of corneal endothelial cell segmentation has also been put by the team of Ruggeri. Their approaches include: applying an artificial neural network to classify pixels as cell contour or cell body [15,16], cell shape modeling using a priori knowledge about position, size, shape, and cardinality incorporated into Bayesian framework [17], labeling each pixel as cell vertex, side, or body using support vector machines classifier [18], and evolving population of vertices forming regular hexagons into cell boundaries using genetic algorithm [19]. Each of the Ruggeri's team's solution is more accurate than the previous ones, however in the case of their newest approach the differences between the manual estimation and the contour obtained automatically still cannot be neglected [19].

The most recent approach to corneal endothelium image segmentation proposed by Katafuchi and Yoshimura [20] bases on a convolutional neural network. Although this kind of approaches

can be very accurate, they require an extensive training on large datasets which can sometimes take days or weeks. This is also in the case of the Katafuchi and Yoshimura's approach. Additionally, since their approach classifies each pixel separately it still suffers from problems related to pixel-based processing and needs postprocessing and due to filter-like application deteriorates segmentation quality at the image borders.

There also exists commercial software for an automatic analysis of corneal endothelial cell morphometric parameters. These include NAVIS by Nidek Technologies or IMAGEnet by Topcon Medical Systems. However, as reported by some authors (e.g., [21]) the software yields a modest to very substantial overestimation. Therefore, even the most recent studies still involve manual delineation of cell boundaries [22].

Having in mind the above-mentioned limitations, this paper proposes a solution to an automatic segmentation of corneal endothelium images. The proposed approach combines a feed-forward neural network which is thought to recognize pixels located at the cell boundaries, with iterative morphological post-processing of the resulting boundary probability map. In contrary to the existing approaches, instead of concentrating on cell boundaries detection, the method first aims at extracting cell bodies by applying the steps described in the following section.

2. Material and method

2.1. Input data

The approach presented in this paper was developed for a publicly available dataset of 30 images of corneal endothelium obtained from commercially slaughtered pigs [16,23]. The images, each of size 576×768 pixels, were acquired at $200 \times$ magnification from 30 porcine eyes stained with alizarine red using inverse phase contrast microscope (CK 40, Olympus) and analog camera (SSC-DC50AP, Sony) and stored as JPEG (RGB) files. For each image, the corresponding manually created ground truth was provided. On average the area of $0.54 \pm 0.07 \text{ mm}^2$ per cornea was assessed, ranging from 0.31 to 0.64 mm^2 . This corresponds to the number of cells ranging from 250 to 480 per region of interest. The size of cells in all images was comparable. This dataset is referred in this study as Dataset 1.

The proposed method was also tested on two other datasets, referred later in the text as Dataset 2 and Dataset 3.

The Dataset 2 was described in [24,11] and made available under the CC BY 3.0 License in [11]. It consists of 30 specular microscopy images of corneal endothelium together with the corresponding ground truth segmentation. The size of each image was 152×388 pixels. The images were stored as grayscale PNG files. The images, obtained from both: healthy and diseased patients, were selected to represent low, medium and high cell densities. The images present cells of various sizes, ranging from 27 to 191 endothelial cells within a field of view.

The Dataset 3 was used by the authors in [25]. It consists of 7 corneal endothelium images of the size ranging from 108×352 pixels to 120×396 pixels and stored as grayscale PNG files. The images were obtained from patients after a cataract surgery. Depending on the image, there were from 59 to 98 cells of similar size within the field of view. Quality of images is low and the contrast at cell boundaries is poor. Images were acquired with a Topcon SP-1000P non-contact specular microscope at the magnification of 150x. Each image was accompanied with manually corrected ground truth boundaries.

The above information about the datasets considered in this study is summarised in Table 1.

Table 1

Summary information of the datasets used in this study.

Dataset ID	No. of images	Resolution [pixels]	File format	Source	Cells in ROI
Dataset 1	30	576 × 768	JPEG (RGB)	phase contrast microscopy	250 ÷ 480
Dataset 2	30	152 × 388	PNG (grayscale)	specular microscopy	27 ÷ 191
Dataset 3	7	from: 108 × 352 to: 120 × 396	PNG (grayscale)	Specular microscopy	59 ÷ 98

2.2. The proposed method

The proposed approach transforms an input corneal endothelium image $I(x, y)$ into a binary image $O(x, y) : \Omega \subset \mathbb{R}^2 \rightarrow \{0, 1\}$ composed of K connected components $R_i = \{(x, y) : O(x, y) = 1\}, i \in [1, K]$ representing endothelial cells and background (i.e., cell boundaries) $R_B = \{(x, y) : O(x, y) = 0\}$ such that $O = [\bigcup_{i=1}^K R_i] \cup R_B$ and $R_i \cap R_j = \emptyset$ for $i \neq j, B$.

This goal is obtained through the procedure briefly summarised in Fig. 1. The main idea behind this procedure is to train a feed-forward neural network N to recognize boundaries between the endothelial cells and then use it to produce edginess map (boundary probability map) P . The map is next adaptively thresholded and recursively processed in order to extract single cells. The consecutive steps of this procedure are described in details in the following subsections.

2.2.1. Image preprocessing

2.2.1.1. Color space transformation and intensity normalization. The datasets considered in this study are inhomogeneous with respect to color representation. Dataset 1 contains RGB images while Dataset 2 and Dataset 3 are composed of grayscale images. Therefore to unify further processing the transformation $H : I \rightarrow I_{HSV}$ is first applied to input images I from Dataset 1. It converts input images $I(x, y) = [r, g, b]$ into the HSV color space, where $I_{HSV} = [h, s, v]$. Further processing is performed with respect to v color component since other colour components do not carry significant information related to endothelial cells.

In the case of grayscale images (like in Dataset 2 and Dataset 3) the intensity is considered. In both cases, the normalization to 8-bit grayscale (i.e. intensities ranging from 0 to 255) is performed prior further processing either with respect to v color component

or with respect to image intensity (which in the case of grayscale images is further also referred as v).

2.2.1.2. Image enhancement. Next the inhomogeneous image intensity distribution is corrected by background removal performed as follows:

$$\hat{v} = v - v_{bkg} \quad (1)$$

where image v_{bkg} of background is obtained via grayscale morphological opening of image v with a big structural element s_{el} as in Eq. (2).

$$v_{bkg} = (v \ominus s_{el}) \oplus s_{el} \quad (2)$$

where \ominus denotes erosion and \oplus stands for dilation.

In this study s_{el} was a disk of a radius equal to 25 pixels. Such element was big enough to remove the cell boundaries. Disk was selected since due to resemblance to the cell shape it diminishes cell shape deterioration. Both, the shape and the size of a structural element were set experimentally.

After the background is removed, the contrast of the resulting image \hat{v} is enhanced using Contrast Limited Adaptive Histogram Equalization (CLAHE) [26] in order to highlight image information at the cell boundaries.

2.2.2. Features determination and network training

The next step assigns to each pixel (x, y) a vector $F = [\hat{v}, \hat{v}, V, V_\sigma]$ of the corresponding features, where: \hat{v} is the average value of \hat{v} in the neighbourhood of 5×5 pixels, V is the vesselness \hat{v} determined using Frangi's approach and V_σ is scale (i.e. the size of vessel-like structures) used for vesselness determination [27]. The Frangi filter was applied with the default parameters setting. Particularly, both weighting parameters α and β were set to 0.5. The considered scales

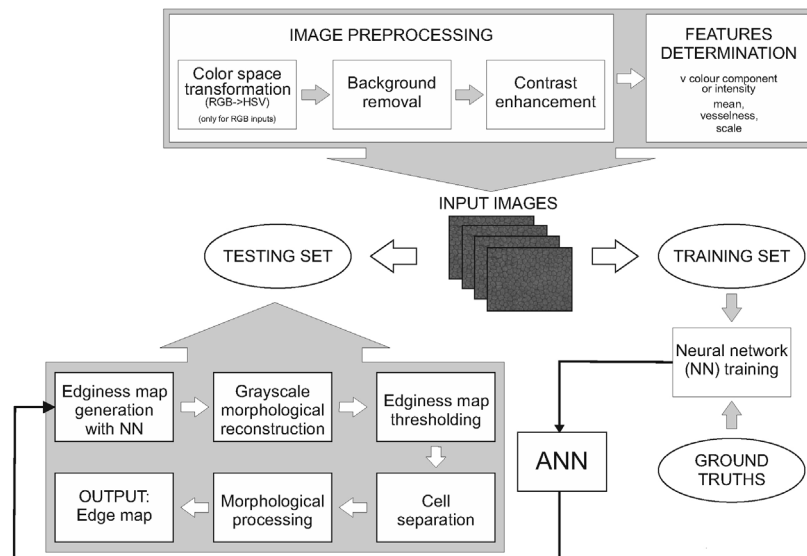


Fig. 1. The overview of the proposed approach.

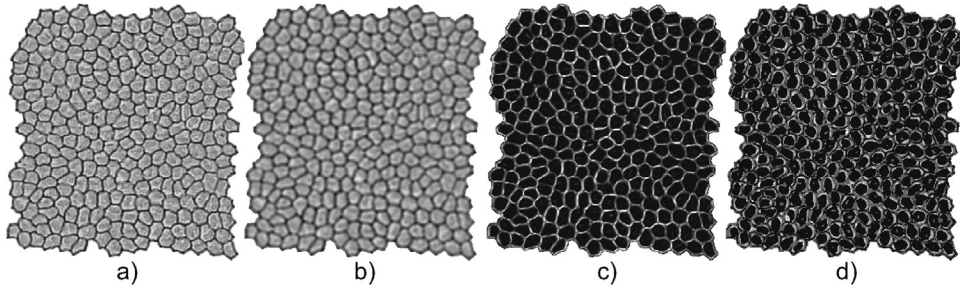


Fig. 2. Features considered during cells segmentation; a) input image after preprocessing v ; b) average \hat{V} ; c) vesselness V ; d) scale V_σ .

ranged from 1 to 10. The scale used as V_σ was the one for which maximum filter response was registered for a particular pixel.

The resulting features obtained for a sample image are presented in Fig. 2.

After the feature vectors F are determined, they are used to train a feed-forward neural network N to distinguish between pixels which do belong and do not belong to the cell boundaries. The trained network outputs for each pixel the probability P that the pixel belongs to the cell boundary, i.e. $N : F(x, y) \rightarrow \{P(x, y) : P(x, y) \in [0, 1]\}$ and the value of 0 corresponds with a cell body while the value of 1 denotes a cell boundary.

The network used in this study consisted of one hidden layer (with tan-sigmoid transfer function) followed by an output layer. There were 10 neurons in the hidden layer and one neuron in the output layer. The outputs of the network were then normalized to be between 0 and 1. The network was trained using Levenberg-Marquardt backpropagation algorithm with the learning rate of 0.01. For training, the ground truth results provided in the dataset were used, after thinning with the BestFit algorithm which moves the boundary skeleton towards the local intensity minima [28]. Both the number of hidden layers as well as the number of hidden neurons within the layer were adjusted in a trial. The training of the network took few seconds (using MATLAB 2015b and NVidia TITAN X GPU).

2.2.3. Boundary probability map processing

The boundary probability map P output by the neural network N visibly highlights cell boundaries (see Fig. 3 b). However, it also highlights regions of the cell nuclei, which in the map P manifest themselves as small bright regions located inside the cells. These regions can disrupt the further cell segmentation. Therefore, their influence is alleviated through grayscale morphological processing performed as follows:

$$P' = \text{fillHoles}(\text{fillHoles}(P) - P); \quad (3)$$

where **fillHoles** denotes hole filling in a grayscale image performed using the algorithm based on morphological grayscale reconstruction described in [29]. Particularly, the dark areas of cells surrounded by lighter borders in the edginess map P are considered as holes. Hole filling procedure makes intensities within cells uniform but also reduces contrast at the cell boundaries. Therefore, in order to keep image contrast high the edginess map P is subtracted from the result of hole filling what causes significant image contrast improvement and highlights cell bodies (see Fig. 3 c). However, as it can be seen from Fig. 3 c in the resulting image there still are brighter regions corresponding with cell nuclei. Therefore, the morphological hole filling is applied once again. As it can be seen from Fig. 3 d, this operation makes cell bodies uniform. However, it also treats some boundaries as holes and reduces the contrast between some cells, thus their separation performed in the next step requires an adaptive procedure.

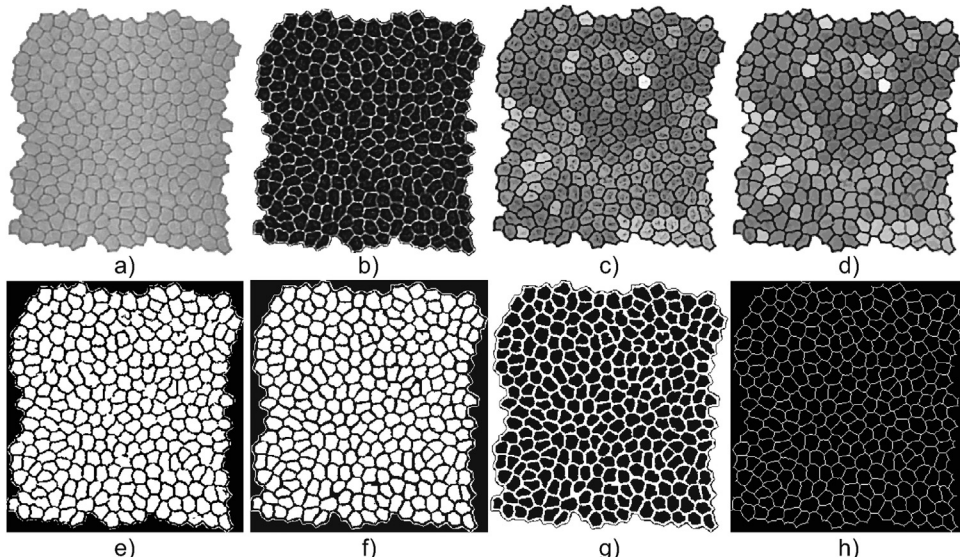


Fig. 3. The consecutive steps of the probability map processing; (a) image intensity \hat{V} ; (b) edginess map P ; (c) the result of morphological reconstruction applied to P ; (d) the result P' of hole filling procedure; (e) binary image B obtained by thresholding of map P' ; (f) the result O of cells separation; (g) inverted binary image O ; (h) cell boundaries S_{SK} .

2.2.4. Cells separation

The last step of the algorithm aims at extracting connected components R_i corresponding to cell bodies. Therefore, image P' is binarised $T : P'(x, y) \rightarrow \{B(x, y) : B(x, y) \in \{0, 1\}\}$ to roughly separate cells from the background. In order to handle varying intensities of cells and decreased contrast at some boundaries, the procedure T of local adaptive thresholding by Sauvola and Pietikäinen [30] is applied. The method determines the threshold t for each pixel following Eq. (4).

$$t = m \left[1 + k \left(\frac{\sigma}{\sigma_{\max}} - 1 \right) \right] \quad (4)$$

where m is mean intensity of the pixel neighborhood, σ is the corresponding standard deviation, σ_{\max} is the dynamic range of standard deviation and k is a positive parameter. In this study, the neighborhood of 15×15 pixels and $k = 0.5$ were used. Both parameters were selected experimentally.

As it can be seen in Fig. 3, in the resulting binary image B there is a group of cells which were correctly separated from the background. However, there is also a significant amount of conjoined cells which need to be separated from each other. Therefore, the iterative procedure was developed to separate cells from the background with the minimal alteration of cell shape. Particularly, in each iteration the separated cells are moved to the output image, while the remaining conjoined cells are gradually disconnected via morphological opening with an increasing structuring element (see Algorithm 1).

Algorithm 1. The algorithm for cells separation

Input: B – binary image, W – image width, H – image height

Output: O – separated cells

```

1:  $\mathcal{O} \leftarrow [0]_{H \times W}$                                 ▷ create an empty output image
2:  $\mathcal{O}' \leftarrow \mathcal{B}$                                      ▷ make the loop run
3: while  $\mathcal{O}' \neq \emptyset$  do                               ▷ as long as there are not separated cells
4:    $\mathcal{O}' \leftarrow [0]_{H \times W}$     ▷ create an image for cells extracted in recent iteration
5:    $\mathcal{B}' \leftarrow \mathcal{B}$                                      ▷ assign an input image to  $\mathcal{B}'$ 
6:    $r \leftarrow 0$                                          ▷ initialize the radius  $r$  of a structural element
7:   while there exist connected components  $R_i$  in  $\mathcal{B}'$  do
8:      $S_r \leftarrow [0]_{r \times r}$     ▷ create disk shaped structural element  $S_r$  of radius  $r$ 
9:      $S_r(\{(x, y) : (x - r)^2 + (y - r)^2 \leq r^2\}) \leftarrow 1$ 
10:     $\mathcal{B}' \leftarrow \mathcal{B}' \circ S_r$     ▷ perform morphological opening of cells using  $S_r$ 
11:    foreach  $R_i \subset \mathcal{B}'$  do    ▷ for each connected component  $R_i$ 
12:       $l_i = \{(x, y) : R_i(x, y) > 0\}$     ▷ select component  $R_i$ 
13:      if  $\text{card}(l_i) \geq T_{size}$  then    ▷ if  $R_i$  is not an outlier
14:        if  $\text{solidity}(R_i) \geq T_{solidity}$  then    ▷ and not conjoined cells
15:           $\mathcal{O}' \leftarrow \mathcal{O}' \cup R_i$     ▷ move  $R_i$  to an output image
16:           $\mathcal{B}(l_i) \leftarrow 0$     ▷ and remove from an input image
17:        end if
18:      else
19:         $\mathcal{B}(l_i) \leftarrow 0$     ▷ clear outliers
20:      end if
21:    end foreach
22:     $r \leftarrow r + 1$     ▷ increase radius  $r$  of a structural element  $S_r$ 
23:  end while
24:   $\mathcal{O} = \mathcal{O}' \cup \mathcal{O}$     ▷ combine results of recent and previous iteration
25: end while
26:  $\mathcal{O} = \mathcal{O} \cup \mathcal{B}$     ▷ include remaining cells to an output image (if any)

```

The proposed approach gradually moves cells from an input image B to an output image O . An input image B may contain both standalone and conjoined cells, while in the output image O there are only standalone cells. This is obtained via the iterative procedure. Particularly, in each iteration connected components R_i corresponding to separated cells are removed from the binary

image B and moved to the output image O . A cell is considered separated if the solidity s (see Eq. (5)) of the corresponding connected component R_i is higher than a threshold $T_{solidity}$.

$$s(R_i) = \frac{|R_i|}{|\text{Conv}(R_i)|} \quad (5)$$

where $\text{Conv}(R_i)$ is a convex hull of connected component R_i and $| \cdot |$ denotes cardinality. In the case of ideal hexagonal shape, the solidity s of a cell equals 1, however, to handle small shape distortions (caused also by morphological processing) the solidity threshold $T_{solidity}$ was set to 0.9.

The remaining connected components R_i of a solidity lower than $T_{solidity}$ are considered as conjoined cells which need to be separated from each other. They remain in image B which is next subjected to image opening with a disk-shaped structural element S_r of radius equal to r . The opening disconnects some cells. These cells are next moved to the output image O . The procedure of image opening and extraction of connected components R_i corresponding to disconnected cells is next repeated based upon the increasing radius r of the structural element S_r until there are no more connected components in the binary image B . In such a case image O contains set of connected components which correspond to cell bodies (see Fig. 3 f). Connected components smaller than T_{size} are treated as outliers and removed, where T_{size} equals to 10% of the average size of the standalone cells disconnected via thresholding. In the first iteration radius r equals 0. This means that morphological processing is not applied since a structural element is empty.

The consecutive steps of cells separation are shown in Fig. 4. The top panel presents binary image B with cells to be separated in the given iteration, while in the bottom panel output image O containing already separated cells is shown. To improve the readability of the figure the cells are shown in random colors. Zoomed parts of the

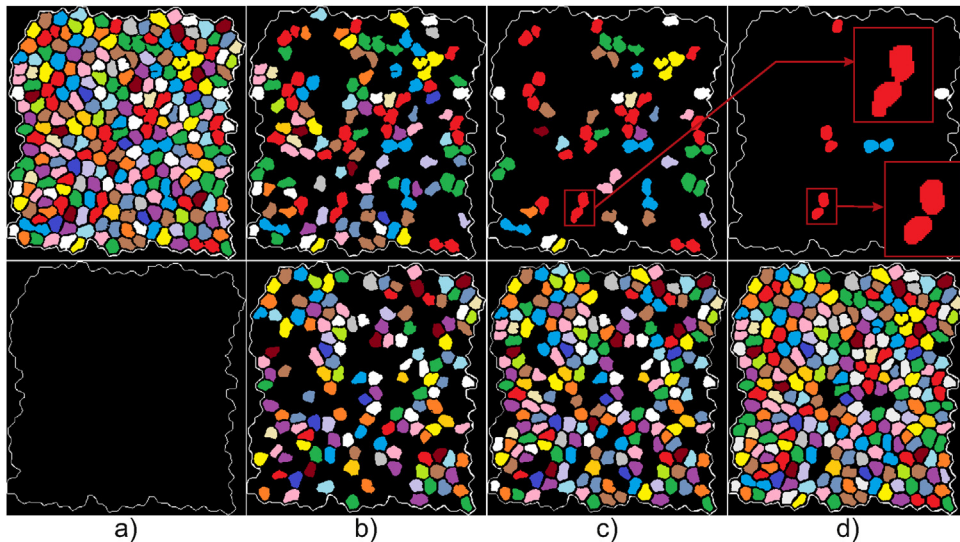


Fig. 4. The consecutive steps of cells separation; top panel – input binary image (cells are shown in colors to improve readability), bottom panel – output binary image (separated cells); (a) the initial state; (b) iteration 2 ($r = 1$); (c) iteration 4 ($r = 3$); (d) iteration 6 ($r = 5$).

image presented in red frames show the result of image opening applied to conjoined cells. The number of iterations is shown in the figure caption. From the Fig. 4 it can be easily seen, how the cells are gradually moved from an input image B (top panel) to an output image O (bottom panel). It can also be observed, that the cells have been properly separated. However, the shape of some cells whose separation required the use of structural elements with higher radii are visibly distorted.

2.2.5. Cell boundaries extraction

The cell boundaries are obtained via skeletisation performed on the inverted image O containing the separated cells (see Fig. 3 g). For skeletonization, the BestFit iterative thinning algorithm [28] was applied.¹ The method moves the boundary skeleton towards the local intensity minima. The resulting skeleton O_{SK} is shown in Fig. 3h.

3. Results

3.1. The assessment of features selection

First, a sequential feature selection [31] was performed to confirm that the features used to build the edginess map are good predictors. Linear discriminant function was applied at this step to fit a multivariate normal density to each group of pixels (i.e. pixels representing cell edges and pixels representing background), with a pooled estimate of covariance. All the considered features were selected in this procedure. The order of feature selection was as follows: vesselness V , intensity \hat{v} , scale V_σ and finally intensity average value \bar{v} . The selected features were next used to train the neural network of the architecture described in Section 2.2.2 to distinguish the cell boundary pixels. In the experiment half of the images was used for training and the other one for testing. The corresponding classification rates obtained for each feature separately as well as for an increasing set of features are shown in Table 2.

The results from Table 2 confirm that the selected features are good predictors since in the case of all datasets they allowed to correctly classify around 80% of cell boundary pixels. The remain-

Table 2

Cell boundary pixels classification rates for the considered feature sets.

Feature set	Dataset 1	Dataset 2	Dataset 3
V	0.76	0.86	0.75
\hat{v}	0.64	0.80	0.62
V_σ	0.60	0.70	0.56
\bar{v}	0.36	0.40	0.41
$[V, \hat{v}]$	0.66	0.85	0.71
$[V, \hat{v}, V_\sigma]$	0.76	0.86	0.75
$[V, \hat{v}, V_\sigma, \bar{v}]$	0.79	0.87	0.81
$[V, \hat{v}, V_\sigma, \bar{v}, \nabla v]$	0.75	0.83	0.77
$[V, \hat{v}, V_\sigma, \bar{v}, \nabla v, \phi_v]$	0.77	0.81	0.74
$[V, \hat{v}, V_\sigma, \bar{v}, \nabla v, \phi_v, \sigma_v^2]$	0.77	0.83	0.78

ing 20% of boundary pixels are found through the cell separation procedure.

It should be also highlighted, that feature selection strongly influences the result of endothelial cells segmentation. Especially, although the resulting edginess map P looks similar to the image of vesselness V when used alone, the latter one provides significantly worse cells segmentation result. This is depicted in Fig. 5.

In the experiment other features were also considered. Particularly, the variance of image intensity σ_v^2 , gradient magnitude ∇v and gradient orientation ϕ_v were additionally considered for each pixel, since these features usually relate to edges in digital images. However, none of these features were selected in the sequential feature selection procedure. Additionally, when included into the feature vector they decreased the neural network classification rates (see Table 2).

3.2. Results on three datasets

The verification of the proposed approach was performed using the leave one out cross-validation procedure performed for each dataset separately. Particularly, the image to be segmented was considered as a testing set. The remaining images were considered a training set and used to train neural network N to produce edginess map P for the tested image. The map P was next processed according to the workflow described in Sections 2.2.3–2.2.5. Finally, the results O_{SK} of cells segmentation were compared with the corresponding ground truth results G . The comparison included three important issues. First, the level of alignment between the ground

¹ <http://home.agh.edu.pl/~pioro/bestfit/>.

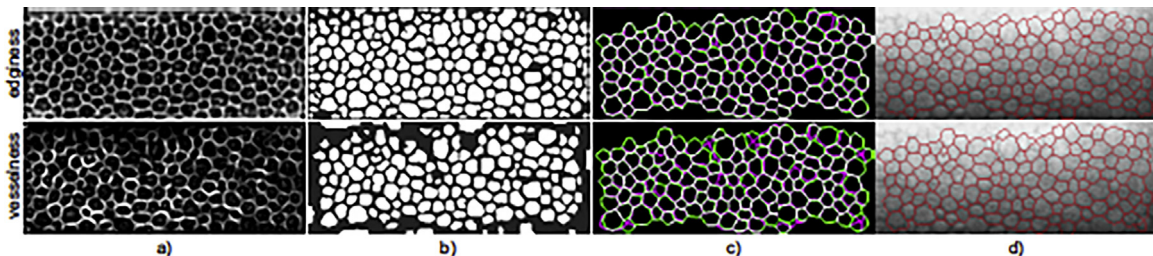


Fig. 5. The difference between cell segmentation results for the edginess P (top panel) and the vesselness V (bottom panel); (a) input map; (b) the extracted cells; (c) the resulting boundaries (in magenta) compared with ground truth boundaries (in green), correctly detected boundaries are shown in white; (d) the resulting boundaries overlaid on the original image.

truth boundaries G and cell boundaries O_{SK} (both postprocessed by the BestFit method [25]) was compared by means of DICE measure (DIC). During the assessment, cell boundary pixels were considered as an object. Only the boundaries in the region under the ground truth were considered in the comparison.

Next, the number n of cells in the segmentation result and the ground truth image n_{GT} , as well as the corresponding average cell sizes \bar{S} and \bar{S}_{GT} measured in pixels were determined and compared by means of the corresponding relative errors δ_n and $\delta_{\bar{S}}$. Finally, evaluation in a direct link with the clinical objectives was performed by means of cells morphometric parameters. Particularly, the coefficient of variations in the area size (CV), cell hexagonality (polymegethism, H) and the average coefficient of variation of cell side length (CVSL) were determined from the segmentation results and related to their counterparts determined from the expert ground truth annotations. Following the definitions in [16,25], to assess the pleomorphism H , the number of neighboring cells for each cell was determined and the percentage of cells with hexagonal shape was taken (see Eq. (7)). For determination of CV and CVSL formulas given by Eqs. (6 and 8) were used.

$$CV = 100\% \frac{1}{\bar{S}} \sqrt{\frac{1}{n} \sum_{i=1}^n (S_i - \bar{S})^2} \quad (6)$$

where S_i denotes area of the i th cell, n stands for the number of cells, \bar{S} is the average area of cells in the image.

$$H = 100\% \frac{n_{hex}}{n} \quad (7)$$

where n_{hex} stands for the number of hexagonal cells, i.e. the cells which are neighbors to six other cells.

$$CVSL = \frac{1}{n} \sum_{j=1}^n \frac{1}{\mu_{SL}} \sqrt{\frac{1}{n_L} \sum_{i=1}^{n_L} (l_i - \mu_{SL})^2} \quad (8)$$

where l_i is the length of i -th side of j -th cell, μ_{SL} is the average length of all sides of j -th cell and n_L is the number of sides.

Values of the above parameters were next compared to their counterparts determined from the ground truth results. The comparison was performed by means of the corresponding relative errors, namely δ_{CV} , δ_H and δ_{CVSL} .

The visual results of the proposed approach applied to the considered datasets are shown in the following figures: for Dataset 1 in Fig. 6, for Dataset 2 in Fig. 7 and for Dataset 3 in Fig. 8. Each figure presents an original image I (a), cells segmented using the proposed approach O (b), boundaries between cells O_{SK} overlaid on the original image I (c) and compared with the ground truth results G (d). For each dataset, the best result (top panel), the average case (middle panel) and the worst result (bottom panel) are shown. The corresponding values of cell segmentation quality measures are given in Table 3.

The numerical assessment of cell segmentation accuracy is presented in Figs. 9–12 and Table 4. Particularly, the results for Dataset 1 are given in Fig. 9 which compares the detected number of cells n with the ground truth n_{GT} number of cells (a) and the determined average cell size \bar{S} with the ground truth average cell size \bar{S}_{GT} (b). Results for each image within the dataset are shown. Similar comparisons for Dataset 2 and Dataset 3 are given in Figs. 10 and 11 respectively.

The distributions of DICE measure and the relative errors of cells morphometric parameters are shown in box plots in Fig. 12 and averaged in Table 4.

3.3. Comparison with other methods

The proposed approach (referred as proposed) was also compared with the selected state-of-the-art methods. The comparison included methods representing the main groups of approaches to segmentation of corneal endothelium images. Particularly, the group of shape-based approaches was represented by the KH algorithm [6] (referred as KH). The stochastic watershed approach [12] (referred as SW) represented the group of watershed-based methods. The machine learning methods were represented by the approach by Gavet and Pinoli [24] (referred as Gavet) and the approach by Katafuchi and Yoshimura [20] (referred as Katafuchi). The first one was the classical approach to machine learning while the latter, the latest one based on a convolutional neural network (CNN). The comparison included the results obtained for all three considered datasets.

The results of KH algorithm were obtained using the software provided by the author with the default parameters setting. Similarly, to generate results of the approach described in [24] the C/C++ source code provided by the author was used. The algorithm was executed with the optimal parameters setting as proposed in [11]. Both algorithms executed in less than a second per image. The SW algorithm was executed using the Matlab code available on-line.² The optimal values of parameters defined in [12] were used. The running time was few seconds per image. The approach proposed by Katafuchi and Yoshimura in [20] was reimplemented (based on the description) for the purpose of this comparison. Python 3.6 programming language and the Keras library were used at this step. Since this method requires training, Dataset 2 was divided into two equal subsets. First, images denoted by even numbers were used to train the CNN which was next used to segment images denoted by odd numbers. Next subsets were reverted and the procedure was repeated. Both times the network was trained for 250 epochs using a total of 200,000 patches of size 64×64 pixels (as suggested in [20]) randomly extracted from the training sets. No data augmentation techniques were applied. Training of each network took about 3 days (c.a. 1000 s per iteration) on a GPU (Nvidia Titan X,

² <http://www.cb.uu.se/~cris/endothelium.html>.

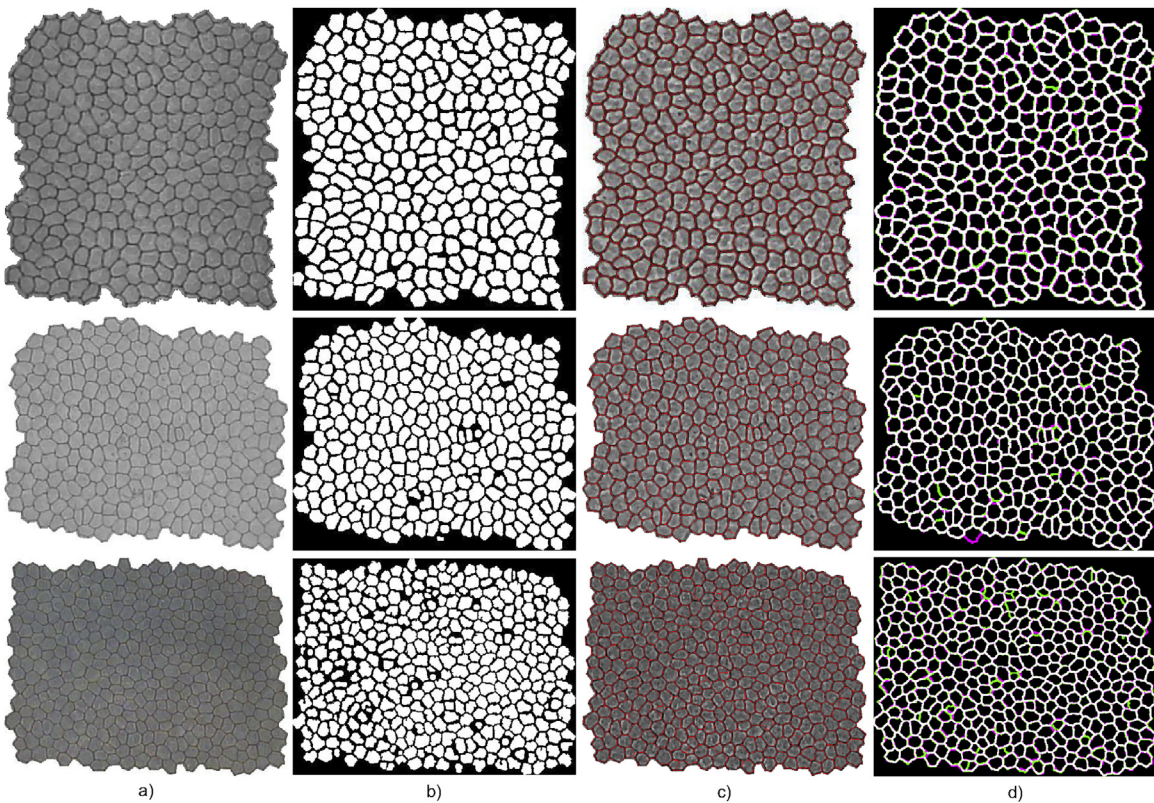


Fig. 6. The results of the proposed approach on Dataset 1; top panel – the best case; middle panel – an average case; bottom panel – the worst case; (a) original image; (b) segmented cells; (c) cell boundaries overlaid on the original image; (d) cell boundaries (in green) compared with the ground truth (in magenta), matching boundaries are shown in white. (For interpretation of the references to color in text/this figure legend, the reader is referred to the web version of the article.)

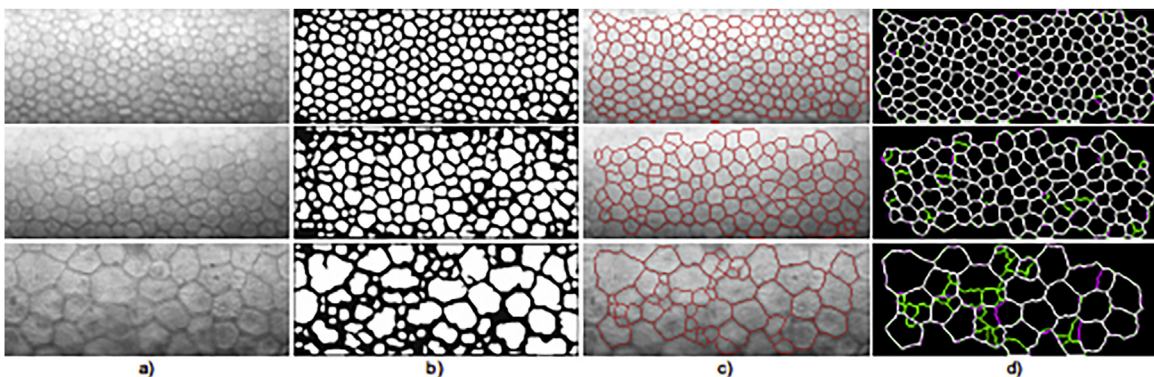


Fig. 7. The results of the proposed approach on Dataset 2; top panel – the best case; middle panel – an average case; bottom panel – the worst case; (a) original image; (b) segmented cells; (c) cell boundaries overlaid on the original image; (d) cell boundaries (in green) compared with the ground truth (in magenta), matching boundaries are shown in white. (For interpretation of the references to color in text/this figure legend, the reader is referred to the web version of the article.)

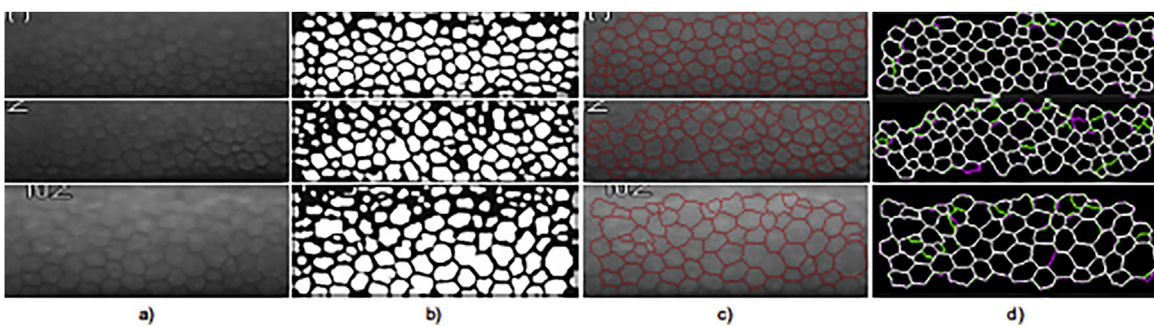


Fig. 8. The results of the proposed approach on Dataset 3; top panel – the best case; middle panel – an average case; bottom panel – the worst case; (a) original image; (b) segmented cells; (c) cell boundaries overlaid on the original image; (d) cell boundaries (in green) compared with the ground truth (in magenta), matching boundaries are shown in white. (For interpretation of the references to color in text/this figure legend, the reader is referred to the web version of the article.)

Table 3

The selected values of cell segmentation accuracy measures corresponding with the cases shown in Figs. 6–8.

Dataset ID	Case	DIC [-]	δ_n [%]	δ_S [%]	δ_{CV} [%]	δ_H [%]	δ_{CVL} [%]
Dataset 1 (see Fig. 6)	best	0.98	0.38	0.1	43.59	2.22	0.38
	average	0.98	1.42	1.57	35.46	4.65	2.72
	worst	0.98	5.77	5.52	22.79	2.04	2.53
Dataset 2 (see Fig. 7)	best	0.97	0.52	0.41	9.93	2.98	2.10
	average	0.91	12.50	12.19	53.93	8.00	14.35
	worst	0.76	100.00	52.86	168.37	33.33	49.22
Dataset 3 (see Fig. 8)	best	0.91	1.23	0.03	6.52	10.04	4.61
	average	0.84	7.14	5.76	35.93	26.66	5.95
	worst	0.87	13.56	11.63	88.42	14.54	5.51

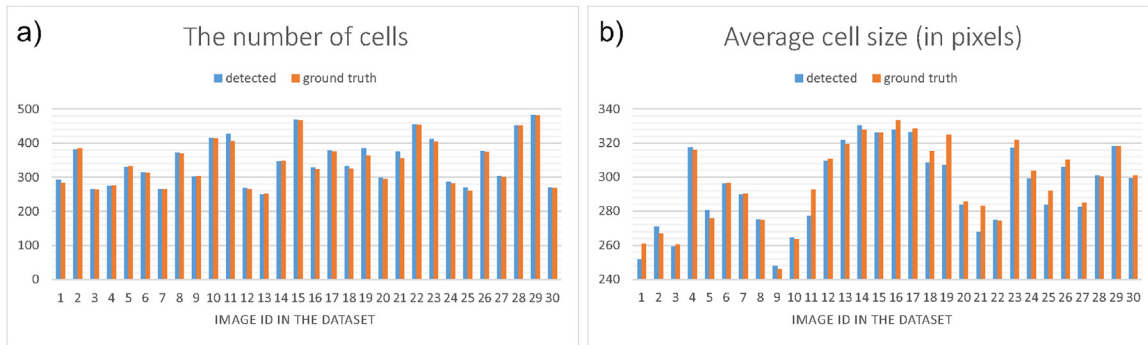


Fig. 9. The numerical assessment of cell segmentation accuracy for each image from Dataset 1; (a) comparison of the detected number of cells; (b) comparison of the average cell size.

Table 4

The comparison of the performance of the considered algorithms for the corneal endothelium image segmentation.

Dataset	Method	DIC [-]	δ_n [%]	δ_S [%]	δ_{CV} [%]	δ_{CVL} [%]	δ_H [%]
Dataset 1	KH	0.96	14.42	12.64	35.77	12.18	14.24
	SW	0.96	7.17	8.35	57.48	5.10	6.10
	Gavet	0.97	7.82	7.93	19.20	8.48	9.01
	Katafuchi	0.97	6.10	5.97	25.30	8.13	9.83
	Proposed	0.97	1.43	1.38	20.84	3.65	5.05
Dataset 2	KH	0.89	33.09	7.55	65.03	23.29	21.32
	SW	0.87	29.27	42.88	24.18	21.03	13.23
	Gavet	0.86	14.74	14.03	70.43	18.70	20.02
	Katafuchi	0.88	12.87	7.55	47.55	7.71	14.24
	proposed	0.90	12.36	8.98	42.37	7.69	16.66
Dataset 3	KH	0.90	27.39	23.35	46.06	23.56	23.41
	SW	0.73	32.49	81.38	28.07	26.83	24.03
	Gavet	0.78	23.97	17.41	81.18	9.21	16.69
	Katafuchi	0.89	2.33	7.74	26.28	9.80	14.25
	Proposed	0.91	5.77	4.68	23.54	5.82	18.35
Average	KH	0.92	24.13	11.48	49.95	18.34	18.37
	SW	0.89	19.71	31.44	39.50	14.50	11.17
	Gavet	0.90	12.61	11.65	48.61	13.14	14.74
	Katafuchi	0.92	8.74	6.86	35.36	8.12	12.27
	Proposed	0.93	6.78	5.13	30.76	5.69	11.64

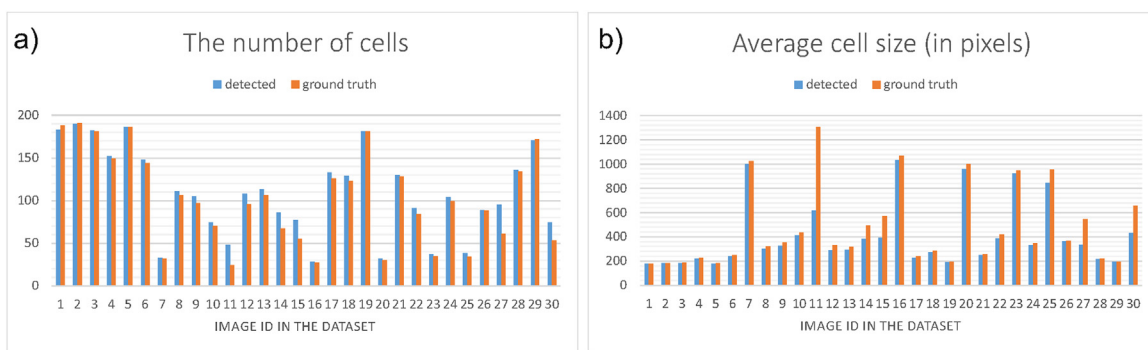


Fig. 10. The numerical assessment of cell segmentation accuracy for each image from Dataset 2; (a) comparison of the detected number of cells; (b) comparison of the average cell size.

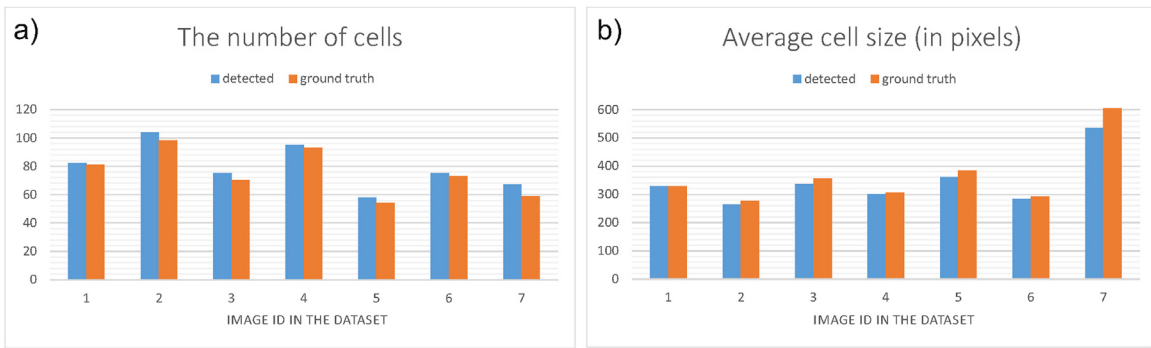


Fig. 11. The numerical assessment of cell segmentation accuracy for each image from Dataset 3; (a) comparison of the detected number of cells; (b) comparison of the average cell size.

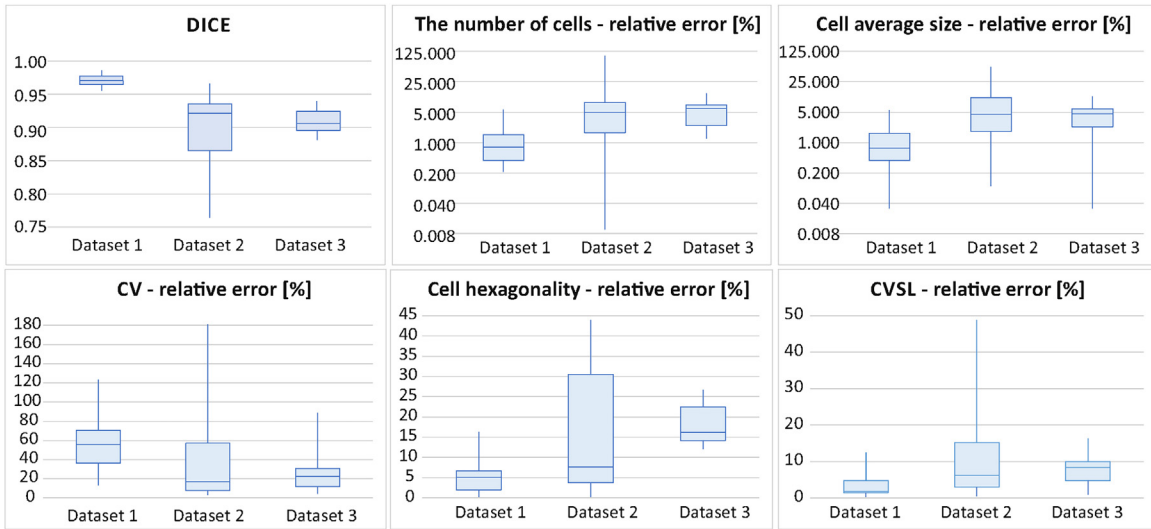


Fig. 12. The distribution of DICE and the relative errors of cell morphometric parameters over the datasets.

12GB GDDR5). Prior comparison, boundaries provided by each considered method were post-processed using the BestFit algorithm [28].

The visual comparison of the results provided by the considered methods for a sample corneal endothelium images composed of cells of various sizes is presented in Fig. 13. The consecutive rows correspond with different methods which names are given in the row captions.

The numerical comparison of the considered methods is shown in Figs. 14–16. Particularly, the distributions of DICE and the relative errors of cell morphometric parameters determined from segmentation results of the considered state-of-the-art methods on Dataset 1, Dataset 2 and Dataset 3 are shown in Figs. 14–16 respectively. The resulting average values of the considered accuracy measures are compared in Table 1.

4. Discussion

The presented results clearly show that the proposed approach performs reasonably well for most of the corneal endothelium images included in the considered datasets. Based on the visual assessment of Figs. 6–8 it can be easily seen that the resulting cell boundaries are well aligned with the corresponding ground truths. This is also confirmed by the DICE measure on average equal to 0.93. This is a good result, especially having in mind that the compared boundaries are thin and even a slight boundary displacement

diminishes DICE value, not necessarily meaning that the cell segmentation failed. The average absolute error δ_n of the determined cell number is below 7% while the corresponding error δ_S of the average cell size is less than 5.2%.

From Figs. 9–11 it can be seen that the proposed approach mostly overestimates the number n of cells. This causes underestimation of the average cell size S . However, it should be also noticed that on average only 5 cells were erroneously divided (ranging from 1 to 24) which can be fast and easily corrected manually.

The average errors of cell morphometric parameters vary depending on the parameter. The average error of cell hexagonality δ_H equals to 11.64%. This is a good result having in mind, that erroneous segmentation of one cell may influence hexagonality of its 6 neighbors. The average error of the coefficient of variation of cell side length (δ_{CVSL}) is only at the level of 5.69%. The highest error (30.76% on average) was observed for the coefficient of variation of cell size. However, from the boxplots in Fig. 12 it can be seen, that the average values of the above parameters are strongly influenced by few erroneous cases and the corresponding median values of the above errors are significantly lower.

The accuracy of the proposed method varies depending on the dataset. The best results were obtained for Dataset 1. As shown in Fig. 12, for all images the DICE measure was closest to 1. This indicates almost perfect alignment between the detected and the ground truth boundaries. The corresponding relative errors δ_n and δ_S were the lowest; both on average below 1.5%. This corresponds

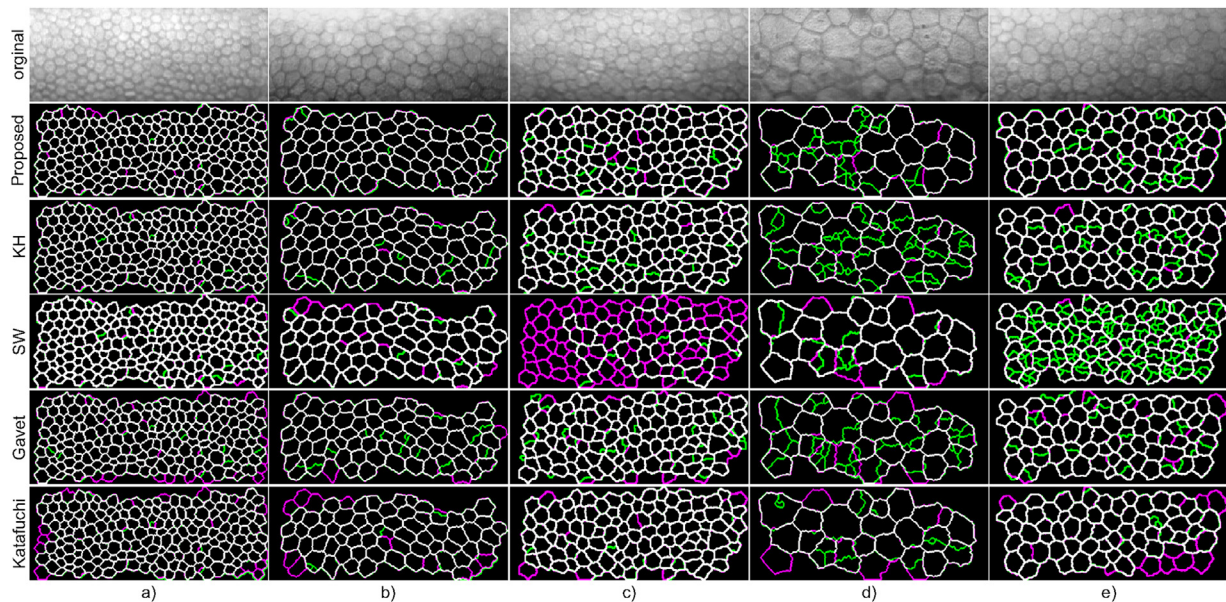


Fig. 13. The comparison between the ground truths and segmentation results provided by various approaches to corneal endothelium image segmentation (white color – correctly detected boundaries, magenta color – missing boundaries, green color – false boundaries).

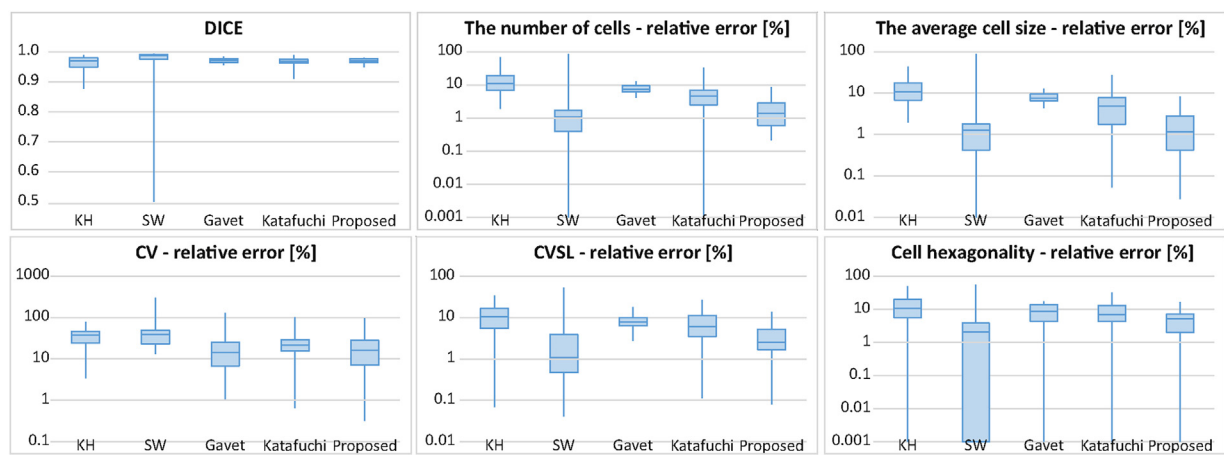


Fig. 14. The distribution of cell segmentation accuracy measures of the selected methods obtained on the Dataset 1.

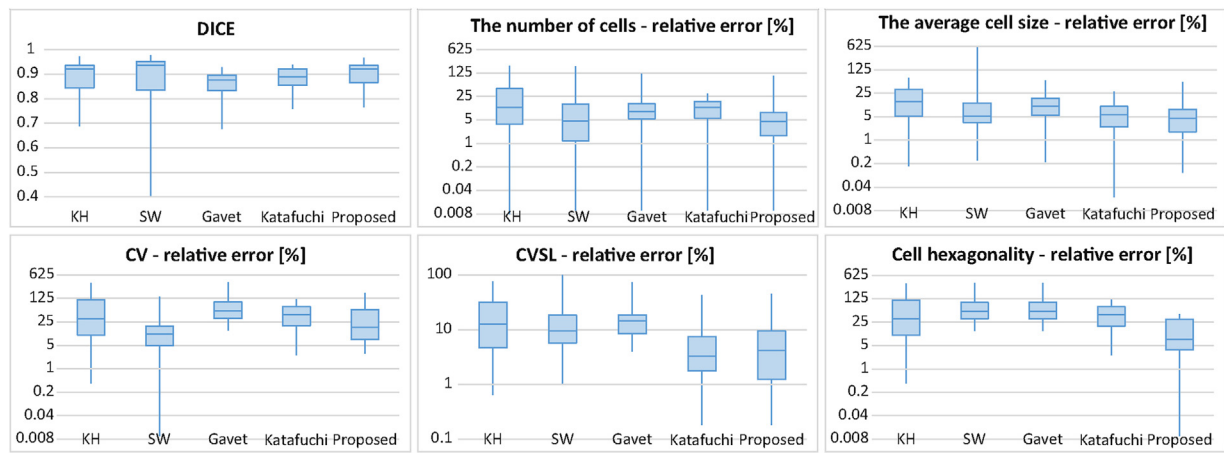


Fig. 15. The distribution of cell segmentation accuracy measures of the selected methods obtained on the Dataset 2.

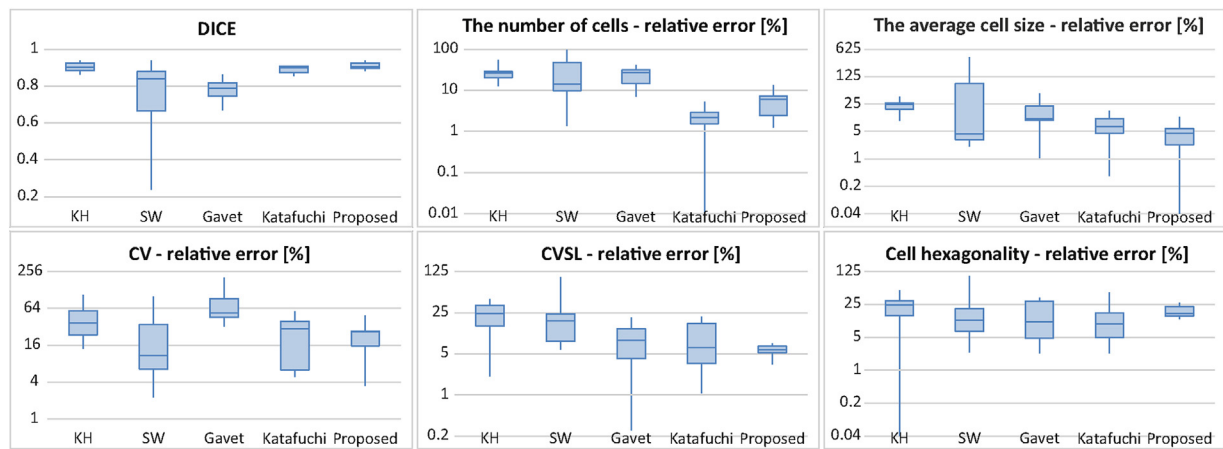


Fig. 16. The distribution of cell segmentation accuracy measures of the selected methods obtained on the Dataset 3.

to 2–3 missing or false boundaries per image. Also, CVSL and cell hexagonality were determined with the lowest errors (3.65% and 5.05% respectively) for the Dataset 1. It is also worth mentioning that each of the considered approaches to corneal endothelium image segmentation performed best in the case of Dataset 1.

When assessed by means of image segmentation accuracy and the determined cells morphometric parameters the proposed method performed worst in the case of Dataset 2. For this dataset segmentation accuracy measures were the lowest (see Table 4). The errors of the determined number of cells δ_n and the average cell size δ_S were the highest and on average equal to around 12% and 9% respectively (see Fig. 12). This means that for this dataset the highest over-segmentation appeared. However, it is also noticeable, that among the results there are cases which are very good (DICE around 0.97, both δ_n and δ_S below 0.5%), as well as the cases which manifest significant over-segmentation (see Figs. 7, 10). The analysis of the results reveals, that the proposed method performed best for images containing many but small cells. The worst results were obtained for images with nonuniform background illumination and few but large cells. The measures of cell segmentation accuracy obtained for Dataset 3 are slightly better than those obtained for Dataset 2. Additionally, most of the cell morphometric parameters were determined with significantly lower errors (see Table 4). The results for Dataset 3 also show that the proposed approaches perform reasonably well in the case of low contrast images.

The comparison of the proposed approach with the state-of-the-art methods is not straightforward. When assessed by the global average values of the considered accuracy measures, the proposed approach performs best, providing the highest average DICE and the lowest average errors of most morphometric parameters (see Table 4). Slightly worse results were obtained for the method by Katafuchi and Yoshimura while the KH and SW approaches performed significantly worse.

When the average values of accuracy measures for each of the datasets are considered, the assessment slightly differs. For Dataset 1 the proposed method visibly outperforms other considered approaches, providing the lowest (and substantially lower than their counterparts) errors of cells morphometric parameters. This is also confirmed by the boxplots in Fig. 14 which show that the errors for the considered approach are both – the lowest and spread less than for the other considered approaches. From the point of view of image segmentation accuracy measures, the proposed approach is also the most accurate on the Dataset 2 achieving the highest DICE among all the considered methods. The corresponding average error of the number of cells is also the lowest for the proposed method and equals to 12.36%. Only a slightly worse value of

the δ_n (i.e. 12.87%) was obtained for the CNN-based approach. The highest over-segmentation appeared in the case of the KH approach, resulting in the error of the determined number of cells δ_n at the level of 33%. Similar error at the level of 30% was also obtained for the SW approach. When compared by means of the cell size error the proposed method is slightly worse than KH approach and CNN-based method by Katafuchi (7.55% vs 8.98%). But from Fig. 15 it can be seen that when outliers are excluded the results by Katafuchi and the proposed approach are nearing, while KH, SW and Gavet approach perform slightly worse. A similar remark can be drawn for CV and cell hexagonality H . The relative errors of these parameters are not the lowest in the case of the proposed method. However, the error distributions of errors show that the lowest median error values were obtained for the proposed approach. Finally, for Dataset 3 the proposed approach performed best in terms of DICE measure and the relative errors of the average cell size, CV, and CVSL. However, the error of the number of cells was lowest for Katafuchi and Yoshimura's method. The remaining methods performed remarkably worse than the proposed approach.

The visual assessment of the results (see Fig. 13) shows that all the considered methods perform best in the case of images presenting small cells, while the worst results are obtained for large cells. In the latter case, all the considered methods suffer from over-segmentation. Results provided by KH algorithm seem to suffer from the largest over-segmentation, while approach by Gavet and Pinoli exhibited moderate over-segmentation. The proposed approach performed slightly better since the number of falsely detected boundaries was less than in the results of KH approach and Gavet's approach. Katafuchi's approach is most resistant to false boundaries but due to a filter-like application, it suffers from lost cells in the outer regions of the image. Another drawback is the very long time required for training. It is also worth noting that the proposed approach exhibits stable performance, especially when compared to the SW approach. The latter method seems to be sensitive to nonuniform background intensity distribution. As a result for one image it provides high-quality results, but for the others totally fails (see Fig. 13). This is not in the case of the proposed method.

In the end, it should be noticed that quantification and comparison of endothelial cell segmentation results by means of morphometric parameters is difficult and not straightforward. As shown and discussed in [25] cell segmentation results (visually assessed as correct) provided by different segmentation approaches lead to significantly different values of cell morphometric parameters. These parameters are very sensitive to misclassified pixels which not necessarily mean that the segmentation failed.

For example, one misclassified pixel influences size of two cells while one wrongly segmented cell influences hexagonality of its six neighbors. The author personally believes that the assessment of cell segmentation accuracy using standard measures (like e.g. DICE) is more reliable than the assessment by means of the morphometric parameters. From this point of view, the results provided by the proposed approach are the most accurate.

5. Conclusion

The approach to corneal endothelium image segmentation was proposed in this paper. The method is fully automatic and is capable of segmenting cells of various shapes and sizes. Even in the case of low contrast images, the resulting cell boundaries are in a good agreement with the ground truth results and require only a limited amount of manual editing. The latter is needed mainly in the case of images containing few large cells in the field of view. In the case of images presenting an area of cornea covered with a high density of small cells, the method performs almost faultlessly.

The method is also universal what was proven by the tests on three distinct and heterogeneous datasets obtained using different devices and acquisition conditions, presenting cells of various characteristics. This is a very good marker of reproducibility and quality of the proposed approach. Also, in some aspects, the method outperforms the state-of-the-art approaches to corneal endothelium image segmentation. Additionally, it is worth noting, that the approach has a limited number of parameters and the results presented in this paper were obtained for the same parameters setting across all three considered datasets. The accuracy of the results could probably also be improved by increasing the size of training dataset since now only a limited amount of images was used for training the neural network to recognize cell boundaries.

All the above issues will be investigated during the future works. However, although the proposed approach to corneal endothelial cells segmentation still requires extensive evaluation on larger datasets, the results presented in this paper should be considered promising and encouraging.

Conflict of interest

None declared.

Acknowledgements

I would like to acknowledge Dr. HDR Yann Gavet from Ecole Nationale Supérieure des Mines de Saint-Etienne for providing a dataset of corneal endothelium images together with the corresponding expert segmentations and the source code of his endothelial cell segmentation algorithm [24,11]. I would also like to thank Dr. hab. Adam Piórkowski from AGH University of Science and Technology for sharing a dataset of corneal endothelium images together with the corresponding manually corrected segmentations and the software implementing KH algorithm [6] and determining cell morphometric parameters.

This work was co-financed by the Lodz University of Technology, Faculty of Electrical, Electronic, Computer and Control Engineering as a statutory activity [Project no. 501/12-24-1-5428].

References

- [1] W. Bourne, Biology of the corneal endothelium in health and disease, *Eye* 17 (8) (2003) 912–918, <http://dx.doi.org/10.1038/sj.eye.6700559>.
- [2] R. Nadachi, K. Nunokawa, Automated corneal endothelial cell analysis, Proc. Fifth Annual IEEE Symposium on Computer-Based Medical Systems (1992) 450–457, <http://dx.doi.org/10.1109/CBMS.1992.245000>.
- [3] F. Sanchez-Marin, Automatic segmentation of contours of corneal cells, *Comput. Biol. Med.* 29 (4) (1999) 243–258, [http://dx.doi.org/10.1016/S0010-4825\(99\)00010-4](http://dx.doi.org/10.1016/S0010-4825(99)00010-4).
- [4] G. Ayala, M. Diaz, L. Martinez-Costa, Granulometric moments and corneal endothelium status, *Pattern Recogn.* 34 (6) (2001) 1219–1227, [http://dx.doi.org/10.1016/s0031-3203\(00\)00074-1](http://dx.doi.org/10.1016/s0031-3203(00)00074-1).
- [5] M. Mahzoun, K. Okazaki, H. Mitsuhashi, H. Kawai, Y. Sato, S. Tamura, K. Kani, Detection and complement of hexagonal borders in corneal endothelial cell image, *Med. Imaging Technol.* 14 (1) (1996) 56–69.
- [6] K. Habrat, M. Habrat, J. Gronkowska-Serafin, A. Piórkowski, Cell detection in corneal endothelial images using directional filters, in: Image Processing and Communications Challenges 7, vol. 389, Springer, 2016, pp. 113–123, http://dx.doi.org/10.1007/978-3-319-23814-2_14.
- [7] L.M. Vincent, B.R. Masters, Morphological Image Processing and Network Analysis of Cornea Endothelial Cell Images, vol. 1769, 1992, pp. 212–226, <http://dx.doi.org/10.1117/12.60644>.
- [8] J. Angulo, S. Matou, Automatic quantification of in vitro endothelial cell networks using mathematical morphology, 5th IASTED International Conference on Visualization, Imaging, and Image Processing (VIIP'05) (2005) 51–56.
- [9] Y. Gavet, J.-C. Pinoli, Visual perception based automatic recognition of cell mosaics in human corneal endothelium microscopy images, *Image Anal. Stereol.* 27 (1) (2008) 53–61, <http://dx.doi.org/10.5566/ias.v27.p53-61>.
- [10] J. Bullet, T. Gaujoux, V. Borderie, I. Bloch, L. Laroche, A reproducible automated segmentation algorithm for corneal epithelium cell images from in vivo laser scanning confocal microscopy, *Acta Ophthalmol.* 92 (4) (2014) e312–e316, <http://dx.doi.org/10.1111/aos.12304>.
- [11] Y. Gavet, J.-C. Pinoli, Comparison and supervised learning of segmentation methods dedicated to specular microscope images of corneal endothelium, *Int. J. Biomed. Imaging* 2014 (704791) (2014) 1–13, <http://dx.doi.org/10.1155/2014/704791>.
- [12] B. Selig, K.A. Vermeer, B. Rieger, T. Hillenaar, C.L.L. Hendriks, Fully automatic evaluation of the corneal endothelium from in vivo confocal microscopy, *BMC Med. Imaging* 15 (1) (2015) 1, <http://dx.doi.org/10.1186/s12880-015-0054-3>.
- [13] D. Issam, E.T. Kamal, Waterballoons: A hybrid watershed balloon snake segmentation, *Image Vis. Comput.* 26 (7) (2008) 905–912, <http://dx.doi.org/10.1016/j.imavis.2007.10.010>.
- [14] K. Charlampowicz, D. Reska, C. Boldak, Automatic segmentation of corneal endothelial cells using active contours, *Adv. Comput. Sci. Res.* 14 (2014) 47–60.
- [15] M. Foracchia, A. Ruggeri, Cell contour detection in corneal endothelium in-vivo microscopy, Proceedings of the 22nd Annual International Conference of the IEEE Engineering in Medicine and Biology Society (Cat. No. 00CH37143), vol. 2 (2000) 1033–1035, <http://dx.doi.org/10.1109/IEMBS.2000.897902>.
- [16] A. Ruggeri, F. Scarpa, M. De Luca, C. Meltendorf, J. Schroeter, A system for the automatic estimation of morphometric parameters of corneal endothelium in alizarine red stained images, *Br. J. Ophthalmol.* 94 (5) (2010) 643, <http://dx.doi.org/10.1136/bjo.2009.166561>.
- [17] M. Foracchia, A. Ruggeri, Corneal endothelium cell field analysis by means of interacting Bayesian shape models, 29th Annual International Conference of the IEEE Engineering in Medicine and Biology Society (2007) 6035–6038, <http://dx.doi.org/10.1109/IEMBS.2007.4353724>.
- [18] E. Poletti, A. Ruggeri, Segmentation of Corneal Endothelial Cells Contour through Classification of Individual Component Signatures, Springer International Publishing, Cham, 2014, pp. 411–414, http://dx.doi.org/10.1007/978-3-319-00846-2_102.
- [19] F. Scarpa, A. Ruggeri, Development of a reliable automated algorithm for the morphometric analysis of human corneal endothelium, *Cornea* 35 (9) (2016) 1222–1228, <http://dx.doi.org/10.1097/ICO.0000000000000908>.
- [20] S. Katafuchi, M. Yoshimura, Convolution neural network for contour extraction of corneal endothelial cells, *Proc. SPIE – Int. Soc. Opt. Eng.* 10338 (2017) 1–7, <http://dx.doi.org/10.1117/12.2264430>.
- [21] S. Jonuscheit, M.J. Dougherty, K. Ramaesh, In vivo confocal microscopy of the corneal endothelium: comparison of three morphometry methods after corneal transplantation, *Eye* 25 (9) (2011) 1130–1137, <http://dx.doi.org/10.1038/eye.2011.121>.
- [22] K. Nurzynska, A. Piórkowski, The correlation analysis of the shape parameters for endothelial image characterisation, *Image Anal. Stereol.* 35 (3) (2016) 149–158, <http://dx.doi.org/10.5566/ias.1554>.
- [23] Laboratory of Biomedical Imaging, BioIMLab, Endothelial cell Alizarine data set, <http://bioimlab.dei.unipd.it/Endo%20Alizara%20Data%20Set.htm>.
- [24] Y. Gavet, J.-C. Pinoli, A geometric dissimilarity criterion between Jordan spatial mosaics. Theoretical aspects and application to segmentation evaluation, *J. Math. Imaging Vis.* 42 (1) (2012) 25–49, <http://dx.doi.org/10.1007/s10851-011-0272-4>.
- [25] A. Piórkowski, K. Nurzynska, J. Gronkowska-Serafin, B. Selig, C. Boldak, D. Reska, Influence of applied corneal endothelium image segmentation techniques on the clinical parameters, *Comput. Med. Imaging Graph.* 55 (2017) 13–27, <http://dx.doi.org/10.1016/j.compmedimag.2016.07.010>.
- [26] K. Zuiderveld, Graphics Gems IV, Academic Press Professional, Inc., San Diego, CA, USA, 1994, pp. 474–485, Ch. Contrast Limited Adaptive Histogram Equalization.
- [27] A.F. Frangi, W.J. Niessen, K.L. Vincken, M.A. Viergever, Multiscale vessel enhancement filtering, in: Vol. 1496 of Lecture Notes in Computer Science, 1998, pp. 130–137, <http://dx.doi.org/10.1007/BFb0056195>.

- [28] A. Piorkowski, Best-fit segmentation created using flood-based iterative thinning, in: R. Choras (Ed.), Image Processing and Communications Challenges 8. IP&C2016, Vol. 525 of Advances in Intelligent Systems and Computing, Springer, Cham, 2017, pp. 61–68, http://dx.doi.org/10.1007/978-3-319-47274-4_7.
- [29] P. Soille, Geodesic Transformations, Springer-Verlag, Berlin, Heidelberg, 1999, pp. 155–183, http://dx.doi.org/10.1007/978-3-662-03939-7_6.
- [30] J. Sauvola, M. Pietikäinen, Adaptive document image binarization, *Pattern Recogn.* 33 (2000) 225–236.
- [31] N.R. Draper, H. Smith, Applied Regression Analysis, 3rd ed., Wiley-Interscience, Hoboken, NJ, 1998.